



Slip-based terrain estimation with a skid-steer vehicle

Giulio Reina and Rocco Galati

Dipartimento di Ingegneria dell’Innovazione, Università del Salento, Via Arnesano, Lecce, Italy

ABSTRACT

In this paper, a novel approach for online terrain characterisation is presented using a skid-steer vehicle. In the context of this research, terrain characterisation refers to the estimation of physical parameters that affects the terrain ability to support vehicular motion. These parameters are inferred from the modelling of the kinematic and dynamic behaviour of a skid-steer vehicle that reveals the underlying relationships governing the vehicle-terrain interaction. The concept of slip track is introduced as a measure of the slippage experienced by the vehicle during turning motion. The proposed terrain estimation system includes common onboard sensors, that is, wheel encoders, electrical current sensors and yaw rate gyroscope. Using these components, the system can characterise terrain online during normal vehicle operations. Experimental results obtained from different surfaces are presented to validate the system in the field showing its effectiveness and potential benefits to implement adaptive driving assistance systems or to automatically update the parameters of onboard control and planning algorithms.

ARTICLE HISTORY

Received 22 October 2015

Revised 17 March 2016

Accepted 11 June 2016

KEYWORDS

Skid-steer vehicles; kinematic and dynamic modelling; terrain estimation; vehicleslippage; model-based estimator

1. Introduction

Current research in robotic mobility aims to develop technologies that allow vehicles to travel longer distances with limited human supervision in highly challenging environments, that is, dynamic outdoor scenarios. While most research on off-road vehicle sensing focuses on obstacle detection, path planning, and position estimation, relatively little attention has been given to the issue of terrain estimation.

Many vehicle control systems, including traction control, stability control, assistive braking, collision warning, cruise control, and adaptive skid-steering can greatly benefit from being ‘terrain adaptive’, that is, the control algorithms can be modified to account for the current terrain properties. For example, it is straightforward that the maximum turning velocity is lower when driving on sand or wet asphalt than on dry asphalt.

Previous work on terrain estimation in mobile robotics mostly relies on the use of exteroceptive sensors, including lidar,[1] vision,[2,3] and radar.[4] Recent research has also focused on terrain sensing based on proprioceptive sensors. For example, in [5], an online method to estimate terrain cohesion and internal friction angle is proposed, based

on sensory data (mainly from proprioceptive sensors) and terramechanics theory. In [6] an approach is used to correlate motor currents and angular rate of the robot with soil parameters (i.e. slip and coefficient of motion resistance). A method for terrain classification based on vibrations induced in the vehicle structure by wheel-terrain interaction is proposed in [7].

A large body of research exists in the automotive field related to wheel-road friction coefficient estimation. Researchers have tried to use the measurement of vehicle motion to obtain an estimate of tire-road friction. Systems that use longitudinal vehicle dynamics and the concept of ‘slip-slope’ are proposed in [8–10]. Lateral vehicle motion-based systems have also been used. For example in [11], differential GPS signals are employed to estimate tire-road friction during cornering, whereas in [12] GPS and INS measurements are used to estimate tire cornering stiffness and improve vehicle state estimation. Although this technology is mature and first commercial solutions appear on the market, these methods generally apply to good paved roads and are unsuitable for off-highway driving. In addition, they are designed for automotive combustion engine-propelled vehicles that use Ackermann steering in contrast to skid-steering and are much faster than most mobile robots having typical travel speed less than 10 km/h.

This paper presents a method for terrain characterisation using skid-steer vehicles. The system is ‘self-contained’, that is, it does not require any special-purpose equipment to be mounted on the vehicle. Rather, the proposed method uses common onboard sensors, including gyros, encoders, and motor current sensors (serving as wheel torque sensors). The unique advantage of this approach is that it can be applied online during normal driving.

Terrain is characterised using three parameters: the coefficient of longitudinal resistance, the coefficient of lateral resistance, and the slip track. The first two parameters represent the motion resistance incurred by the vehicle on a particular terrain along the longitudinal and lateral direction. They are estimated during straight and turning motion, respectively, by using as sensory input the vehicle attitude provided by an inertial measurement unit and the motor electrical currents drawn by the wheel pair of either vehicle side. The concept of slip track derives from the kinematic modelling of the skid-steering mechanism and it expresses a measure of the amount of slippage incurred by the vehicle in a turn. In order to estimate online the slip track, a model-based estimator using Kalman filtering is adopted that employs as measurement input the difference in the wheel velocities of the right and left side wheels as obtained from rotary encoders and the vehicle yaw rate measured by a gyroscope.

The paper is organised as follows. Section 2 illustrates the kinematics of a skid-steer vehicle, introducing the slip track parameter and its estimation approach. Section 3 describes the vehicle-terrain interaction during straight and turning motion. An analytical solution is also drawn for the weight distribution problem with arbitrary roll and pitch. Experimental results, performed with an all-terrain vehicle on different surfaces, are presented in Section 4 to validate the proposed approach. Section 5 concludes the paper.

2. Kinematics of skid-steer vehicles

Skid-steering is a common turning mechanism used in vehicles where wheels have fixed direction. It is, for example, the main steering mechanism for tracked vehicles. The skid

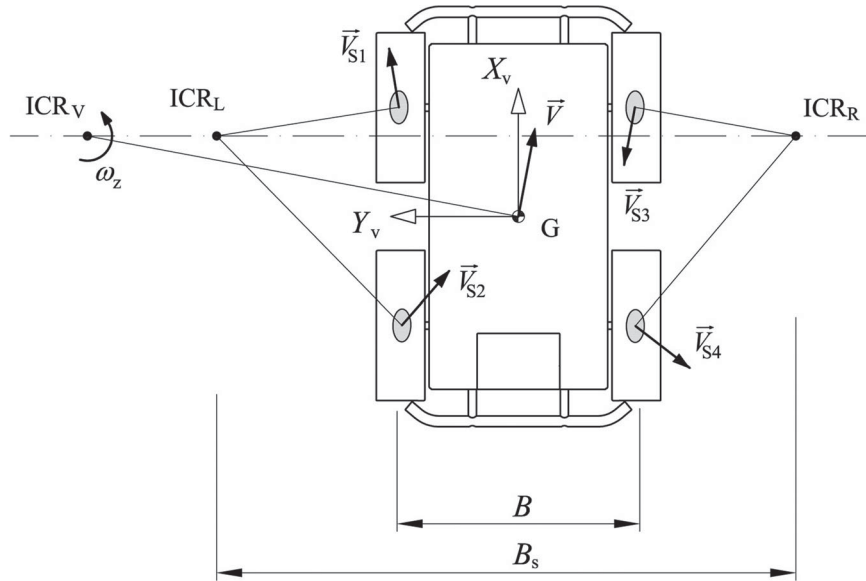


Figure 1. Kinematic model of a skid-steer vehicle. Note that $\bar{V}_{S,i}$ is the slip velocity of the wheel contact patch i with respect to the ground (i.e. the absolute velocity of the contact patch with respect to a fixed inertial reference frame). Positive values of the longitudinal slip velocity indicate that the wheel is dragged, whereas negative values indicate that the wheel is under traction. The slip track B_s is defined as the distance of the side wheel ICRs along the Y_v -axis.

steering principle is based on the generation of differential velocities at the opposite sides of the vehicle. Simplicity, robustness, and turn-on-the-spot capability make skid-steering a common design choice for all-terrain vehicles. However, due to the large amount of skidding experienced by the vehicle during a turn, wheel-terrain interaction is complex and difficult to model, resulting in control and pose estimation issues.

Figure 1 shows the kinematics of a skid-steer vehicle during a counter-clockwise turn with reference to a left-hand vehicle-fixed coordinate system (X_v, Y_v, Z_v) , whose origin is assumed in the vehicle centre of mass. Under the further assumptions of rigid bodies and planar motion, the instantaneous centre of rotation (ICR) of the vehicle, ICR_v , is defined as the point in the motion plane around which the vehicle has a pure rotational motion at a specific instant of time. It is also interesting to observe the behaviour of the side wheels on their contact surface with the motion plane. Each contact patch has a relative motion with respect to the vehicle body, due to the wheel rotation around its axis, and an absolute motion with respect to the ground. Thus, the motion of a wheel tread point can be studied as the composition of the relative motion around the wheel axis and that embedded with the vehicle. As a result, the ICR of the wheel patch is different from the ICR of the wheel rotational axis. The ICRs for the left and right side wheels can be defined in the vehicle frame as $ICR_L = (x_{ICR_L}, y_{ICR_L})$ and $ICR_R = (x_{ICR_R}, y_{ICR_R})$, respectively. Note that, as either side wheel pair is mechanically coupled, the wheel contact patches of the same side admit equal ICR. Interestingly, ICR_L and ICR_R lie on a line parallel to the Y_v -axis, which also contains ICR_v , as stated by the Kennedy-Aronholdt theorem.[13]

Local coordinates for the ICRs of the wheel contact patches along the Y_v -axis can be obtained as a function of the vehicle's angular and linear velocity by applying the principles of relative kinematics,

$$y_{\text{ICR}_L} = \frac{V_{x,L} - V_x}{\omega_z}, \quad (1)$$

$$y_{\text{ICR}_R} = \frac{V_{x,R} - V_x}{\omega_z}, \quad (2)$$

where $V_{x,L}$ and $V_{x,R}$ are the velocities of the left-hand and right-hand side wheels, respectively, with respect to the vehicle reference frame, V_x and ω_z are the x -component of the linear velocity and angular velocity of the vehicle, respectively. By subtracting Equation (2) from Equation (1), it gets

$$B_s = y_{\text{ICR}_L} - y_{\text{ICR}_R} = \frac{V_{x,R} - V_{x,L}}{\omega_z} = \frac{\Delta V}{\omega_z}, \quad (3)$$

where the numerator represents the difference in the input wheel velocities, ΔV . B_s is referred to as the 'slip track' and it represents the distance measured along the Y_v -axis between the side wheel ICRs.

It should be noted that the position of ICR_L and ICR_R (and so the value of B_s) are dynamics-dependent. However, due to the lateral slip incurred by the wheels, they always lie outside the wheel centrelines. The larger B_s , the higher the amount of skidding experienced by the vehicle. For example, ICR_L and ICR_R approach infinity when the robot is stationary but the wheels are spinning. This may occur when the vehicle drives on a low friction surface or becomes immobile in some way. Therefore, the slip track can be used as a measure of the overall skidding incurred by the vehicle. Difference in the input wheel velocities being equal, the slip track mostly depends on the particular terrain. It can be estimated online by monitoring the vehicle motion through a Kalman filter-based observer, as will be explained in the next section.

The idea of using the ICR for the left and right side wheels was originally used to improve the accuracy of pose estimation systems in skid-steer vehicles, as in [14,15]. In this paper, the slip track concept is introduced as a parameter to characterise the properties of a given terrain under investigation.

2.1. Estimation of slip track using Kalman filtering

In many mechanical systems, it is often difficult to measure all states/parameters that describe the system's behaviour.[16] This is the case for the slip track that cannot be directly measured. However, a 'virtual' sensor or observer can be adopted. The basic idea is that of inferring a physical quantity (i.e. the slip track) that is not directly measurable from existing sensors through the use of a model (i.e. Equation (3)). One important aspect of state estimation is that the system to be observed is usually excited by a stochastic noise w , due for example to imperfections in modelling the system. In addition, sensor readings may be affected by their own stochastic noise v . Therefore, deterministic open-loop models may be of limited validity and stochastic closed-loop observers are necessary. One common solution is the Kalman filter that in the context of this research is applied to the problem of

slip track estimation. The proposed observer is based on the use of one vertical gyroscope measuring the rate-of-turn ω_z and rotary encoders providing the difference in the input wheel velocities ΔV .

In order to estimate the slip track, B_s , Equation (3) can be rewritten as

$$\omega_z = \Delta V \frac{1}{B_s}. \quad (4)$$

The main reason is that the measurement noise variance is much larger for ω_z , that is, $\sigma_{\text{gyro}} = (0.3 \text{ rad/s})^2$, than for ΔV , that is, $\sigma_{\text{encoder}} = (0.5 \cdot 10^{-2} \text{ m/s})^2$. Therefore, the latter uncertainty will be mostly neglected.

To implement a state observer using Kalman filtering, Equation (4) can be extended to a discrete-time state-space model where the parameters values vary like a random walk

$$x_{k+1} = x_k + w_k, \quad (5)$$

$$z_{k+1} = H_{k+1}x_{k+1} + v_{k+1}, \quad (6)$$

where $x_k = 1/B_s$ is the state variable, that is, the inverse of the slip track B_s , at time k , z_{k+1} is the observation, that is, ω_z , and H_{k+1} the measurement coefficient, that is, ΔV , at time $k+1$. The process disturbance and the measurement noise, denoted by w_k and v_k , respectively, are assumed to be zero-mean Gaussian distributions, temporally independent of each other with covariance, respectively, $Q = E[w_k w_k^T]$ and $R = E[v_k v_k^T]$.

R accounts for the uncertainty in the measurement and it is set as $R = \sigma_{\text{gyro}}$. The determination of Q is generally more difficult, since the estimated process cannot be directly observed. As a consequence, the process noise covariance Q is tuned depending on the quality of the developed model. For the proposed observer, more reliance is placed on the model than measurement using a heuristically determined process noise equals to $Q = 10^{-4}(m^{-1})^2$. The sensor output rate is used to define the sampling time of the Kalman observer (i.e. $T_s = 0.01 \text{ s}$).

Kalman filtering estimation operates through the prediction-correction cycle expressed by [17]

Prediction:

$$\hat{x}_{k+1}^- = A_d \hat{x}_k + B_d u_k, \quad (7)$$

$$P_{k+1}^- = A_d P_k A_d^T + Q, \quad (8)$$

Correction:

$$K_{k+1} = P_{k+1}^- H_d^T (H_d P_{k+1}^- H_d^T + R)^{-1}, \quad (9)$$

$$\hat{x}_{k+1} = \hat{x}_{k+1}^- + K_{k+1} (z_{k+1} - H_d \hat{x}_{k+1}^-), \quad (10)$$

$$P_{k+1} = (I - K_{k+1} H_d) P_{k+1}^-, \quad (11)$$

where \hat{x}_{k+1}^- is the predicted state vector, P_{k+1}^- is the variance matrix for \hat{x}_{k+1}^- , K_{k+1} is the gain matrix, \hat{x}_{k+1} is the updated state vector, and P_{k+1} is the updated error covariance estimate.

The slip track estimation is performed during turning maneuvers, whereas the filter is switched off for straight driving due to the lack of excitation. It is worth noting that the slip

track value remains bounded. As the vehicle approaches straight driving, numerator and denominator in Equation (3) are infinitesimals of the same order, resulting in finite values of B_s .

3. Vehicle-terrain interaction

Two methods are presented to estimate the motion resistance experienced by a skid-steer vehicle during straight and turning motion. In both cases, the wheels act as ‘tactile’ sensors that estimate the forces exerted on the terrain by measuring the drive motor currents.

3.1. Longitudinal motion resistance

The free-body diagram of a drive wheel rolling with constant speed on natural ground is shown in Figure 2. Due to energy dissipation occurring in the deformed parts of the tire and possibly the ground, the resultant of the normal stresses acting on the contact patch, F_z , is shifted forward with respect to the centre of contact. As a result, a driving torque, T_r , needs to be applied to overcome the corresponding rolling resistance moment

$$T_r = f_r r F_z \quad (12)$$

f_r being the coefficient of motion resistance of the vehicle in the longitudinal direction, F_z the vertical load acting on the wheel, and r the wheel radius. On paved road, the prevalent of the motion resistance mechanisms is the tire hysteresis caused by the energy dissipated

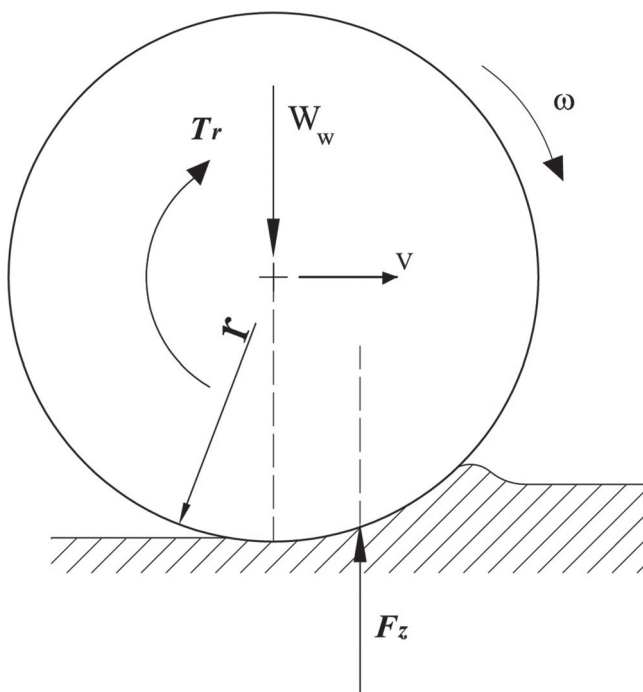


Figure 2. Wheel-terrain interaction model.

by the cyclic deformation of the contact patch. Conversely, the main cause of dissipation on natural road is the mechanical work of soil plastic deformation. According to the terrain properties, rolling resistance can increase of an order of magnitude.[18]

One possible solution to get an estimate of f_r is to measure the electrical current drawn by the wheel drive motor.[19,20] It is known that in DC brushed motors, the electrical current, I , is roughly proportional to the delivered mechanical torque T_r

$$T_r = \tau k_t I, \quad (13)$$

where k_t is the motor torque constant and τ is the gearhead ratio. Therefore, by measuring the motor current during straight driving at constant speed, it will be possible to get an indirect estimate of the motion resistance, given the wheel geometry and the vertical load. Calculation of the vehicle's normal forces on irregular terrain will be discussed in the following section.

3.1.1. Vertical forces.

Wheel loads constantly change during operations on rough terrain. The load distribution can be expressed by the vertical forces that act on each of the four wheels. Since the travel velocity is usually slow (typically less than 1 m/s) in order to reduce shocks and to cope with the high processing time requested by navigation algorithms, a quasi-static model can be assumed for the force analysis where the inertial contributions are neglected and the only external load is the vehicle weight. Such a model can be solved for wheel/terrain contact forces knowing the attitude of the vehicle as it negotiates terrain grade and irregularities. With reference to Figure 3, a world reference frame (WRF) $\{O_g, X_g, Y_g, Z_g\}$, and a vehicle reference frame (VRF) $\{O_v, X_v, Y_v, Z_v\}$ can be defined. The vehicle attitude with respect to the WRF can be expressed in terms of Euler angles. In our system, the RPY convention is chosen. Figure 3 shows the three Euler angles, which are usually referred to as roll (ϕ), pitch (θ), and yaw (ψ), respectively. The transformation relationship from the VRF to the WRF is given by the following matrix

$$R_V^W = \begin{pmatrix} c\psi \cdot c\theta & c\psi \cdot s\theta \cdot s\phi - s\psi \cdot c\phi & c\psi \cdot s\theta \cdot c\phi + s\psi \cdot s\phi \\ s\psi \cdot c\theta & s\psi \cdot s\theta \cdot s\phi + c\psi \cdot c\phi & s\psi \cdot s\theta \cdot c\phi - c\psi \cdot s\phi \\ -s\theta & c\theta \cdot s\phi & c\theta \cdot c\phi \end{pmatrix}, \quad (14)$$

where c and s , refer to cos and sin, respectively.

Figure 4 shows the force analysis of the vehicle on uneven terrain. It is assumed that each wheel makes contact with the terrain at a single point, denoted with P_i , $i = 1, \dots, 4$, that is, distributed wheel-terrain contact stresses can be resolved to resultant forces at a single point. Thus, a wheel-terrain contact force exists at each point P_i and it is denoted with F_i . With respect to the VRF, F_i can be decomposed into a tractive and lateral force $F_{x,i}$ and $F_{y,i}$, and a normal force $F_{z,i}$, that is, $F_i = [F_{x,i}, F_{y,i}, F_{z,i}]^T$. The position vectors p_i are directed from the wheel terrain contact points to the rover centre of mass. In general, the force vector F_s at the vehicle centre of mass represents the summed effects of gravitational forces, inertial forces, forces due to manipulation, and forces due to interaction with the environment or other robots. However, in this analysis only the vehicle weight W is considered, that is, $F_s^W = [0, 0, W, 0, 0, 0]^T$. Then, the quasi-static force balance equations can

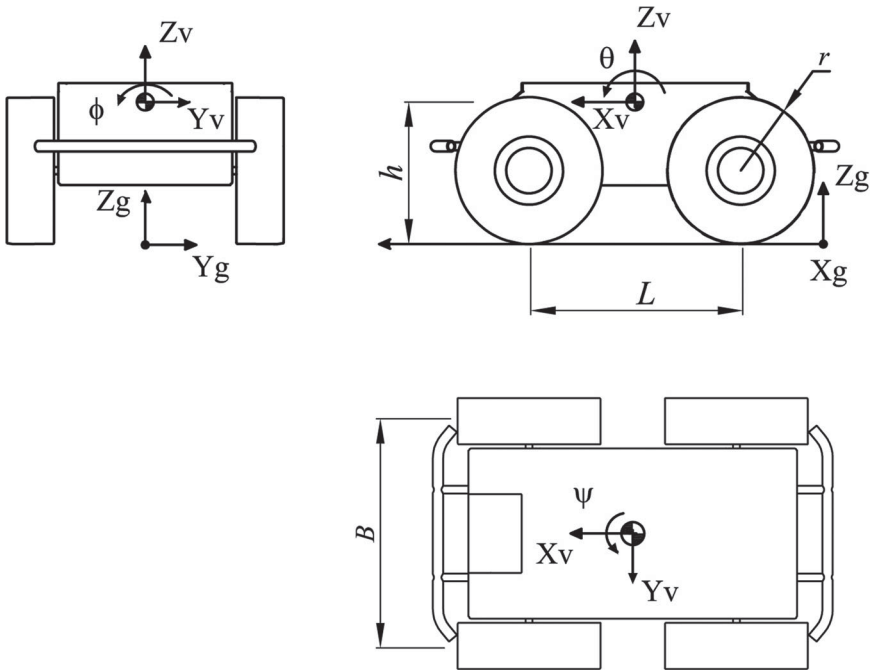


Figure 3. Reference frames and nomenclature for the all-terrain rover.

be obtained as

$$\begin{bmatrix} I & \dots & I \\ 0 & -p_1^z & p_1^y \\ p_1^z & 0 & -p_1^x \\ -p_1^y & p_1^x & 0 \end{bmatrix} \cdot \begin{bmatrix} F_1 \\ \vdots \\ F_4 \end{bmatrix} = F_s, \quad (15)$$

where I represents a 3×3 identity matrix. This set of equations can be written in compact matrix form as

$$G \cdot F = F_s, \quad (16)$$

where the G depends on the vehicle geometry. Equation (16) represents the quasi-static force balance of the vehicle and it is usually referred to as the force distribution equation.[21]

Note that all vectors involved in Equation (14) have to be expressed in the same reference frame. If the VRF is chosen, F_s can be obtained as

$$F_s^V = [(R_V^W)^{-1} 0_{3 \times 3}] F_s^W = \begin{bmatrix} W \sin \theta \\ -W \cos \theta \sin \phi \\ -W \cos \theta \cos \phi \\ 0 \\ 0 \\ 0 \end{bmatrix}. \quad (17)$$

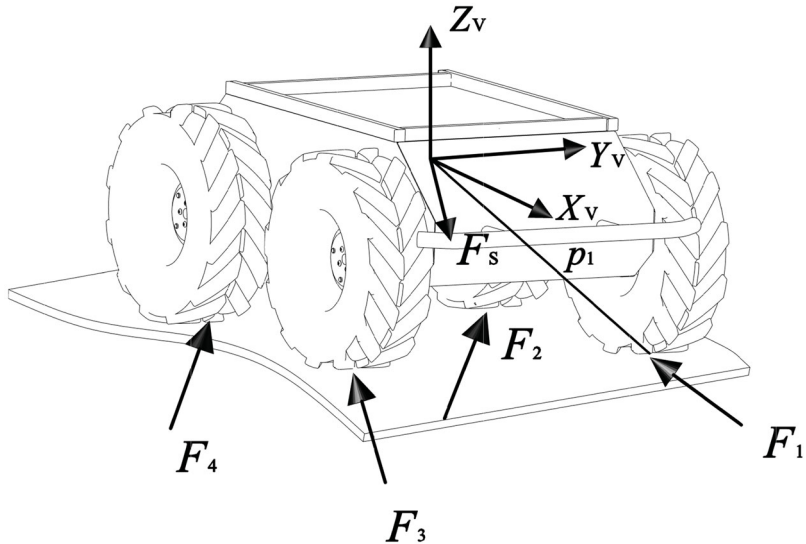


Figure 4. Force analysis of a four-wheel all-terrain rover.

Given the vehicle mass and geometric properties and the attitude, which can be estimated for example using an inertial measurement unit, it is known the input to the problem, F_s . Output are the wheel-terrain contact forces. Under the assumption that all wheels equally contribute to balance the longitudinal and lateral external force, which is reasonable as the centre of gravity approximately coincides with the geometric centre of the vehicle, Equation (16) can be analytically solved for the wheel vertical forces expressed in the VRF

$$F_{z,1} = \frac{W}{4} \cos \phi \cos \theta + \frac{W}{2} \sin \theta \frac{h}{L} - \frac{W}{2} \cos \theta \sin \phi \frac{h}{B}, \quad (18)$$

$$F_{z,2} = \frac{W}{4} \cos \phi \cos \theta - \frac{W}{2} \sin \theta \frac{h}{L} - \frac{W}{2} \cos \theta \sin \phi \frac{h}{B}, \quad (19)$$

$$F_{z,3} = \frac{W}{4} \cos \phi \cos \theta + \frac{W}{2} \sin \theta \frac{h}{L} + \frac{W}{2} \cos \theta \sin \phi \frac{h}{B}, \quad (20)$$

$$F_{z,4} = \frac{W}{4} \cos \phi \cos \theta - \frac{W}{2} \sin \theta \frac{h}{L} - \frac{W}{2} \cos \theta \sin \phi \frac{h}{B}. \quad (21)$$

In conclusion, Equations (18)–(21) provide estimation of wheel vertical forces for an arbitrary roll and pitch angle.

3.2. Lateral motion resistance

Figure 5 shows the overall behaviour of a skid-steer vehicle during a left-hand turn. The thrust of the right side wheels, F_R , is increased, whereas that of the left side wheels, F_L , is reduced, so as to generate a turning moment to overcome the moment of turning resistance, M_r , due to the lateral slip of the wheels on the ground. Under the assumptions of steady-state steering at low speeds, the rotational inertia of the vehicle can be neglected, and the

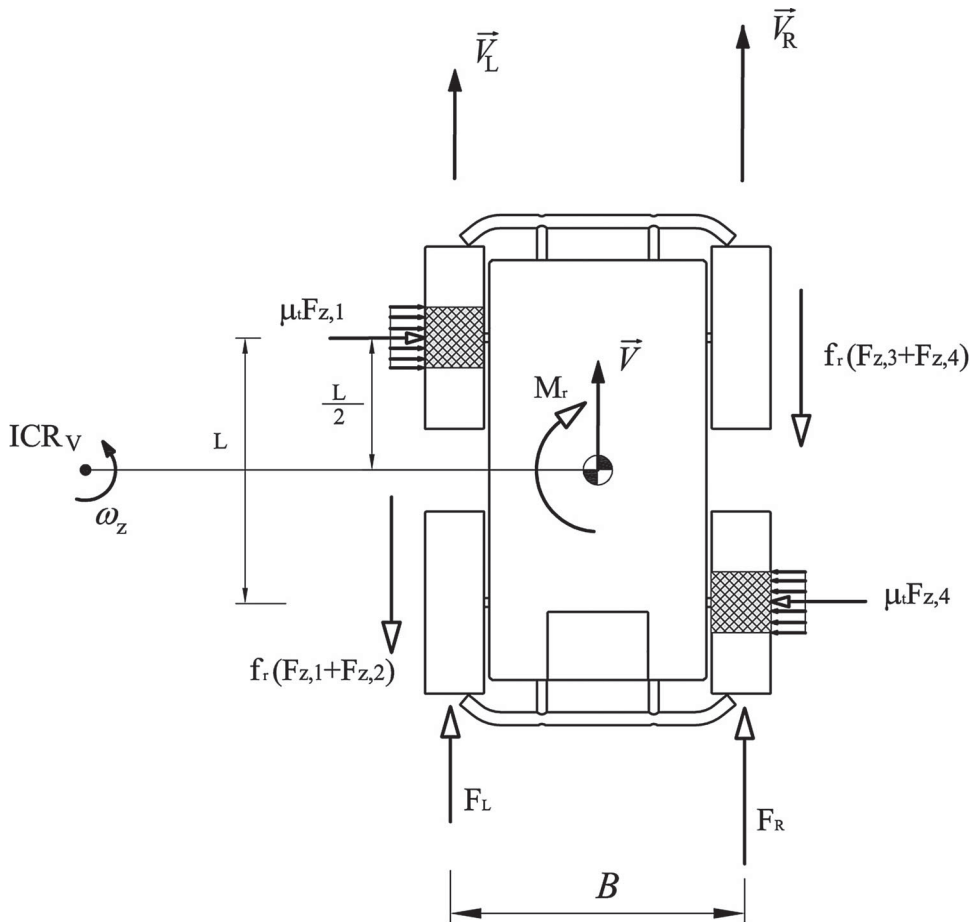


Figure 5. Schematic of a vehicle turning by skid-steering. For simplicity's sake, the diagram of the lateral stresses is reported only for the front left wheel and rear right wheel.

outside and inside thrusts can be expressed as [22]

$$F_L = f_r(F_{z,1} + F_{z,2}) + \sigma \frac{M_r}{B}, \quad (22)$$

$$F_R = f_r(F_{z,3} + F_{z,4}) + \frac{M_r}{B}, \quad (23)$$

where σ in Equation (22) is a sign variable assuming value $\sigma = 1$ for turn-on-the-spot and $\sigma = -1$ for any other turning manoeuvre. f_r is the coefficient of motion resistance in the longitudinal direction, as explained in Section 3.1. In order to account for the lateral slip of the wheels, the coefficient of lateral resistance μ_t can be introduced. Assuming equal value of μ_t for all wheels, the moment of turning resistance can be expressed by (refer to Figure 5)

$$M_r = \frac{\mu_t WL}{2}. \quad (24)$$

Accordingly, Equations (22) and (23) can be rewritten in the following form

$$F_L = f_r(F_{z1} + F_{z2}) + \sigma \frac{\mu_t WL}{2B}, \quad (25)$$

$$F_R = f_r(F_{z3} + F_{z4}) + \frac{\mu_t WL}{2B} \quad (26)$$

and finally an expression for μ_t can be drawn

$$\mu_t = \frac{B}{L} \left(\frac{F_R + F_L}{W} - f_r \right). \quad (27)$$

The higher the moment of turning resistance exerted on the vehicle by the terrain, the larger the power required during a turn with respect to a straight line motion.

As explained in Section 3.1, motor current is known to be related with mechanical torque. Therefore, an indirect measurement of the trust exerted by the particular terrain on the wheels can be obtained through the electrical current readings dividing by the tire radius. Using Equation (12), it was shown that an estimate of f_r can be obtained during straight motion at constant speed. Similarly, μ_t can be measured during turning maneuvers via Equation (27), given the geometry and weight of the vehicle, the motor currents, and the value of f_r .

As for the slip track, it is important to underline that, on first approximation, the influence of velocity is neglected. Thus, different terrains can be compared in terms of B_s , f_r and μ_t , the difference in the input wheel velocities being equal.

In summary, the main result of the aforementioned discussion is that a given terrain can be characterised by three parameters underlying the vehicle/terrain interaction. These parameters are the slip track, the coefficient of motion resistance, and the coefficient of lateral resistance.

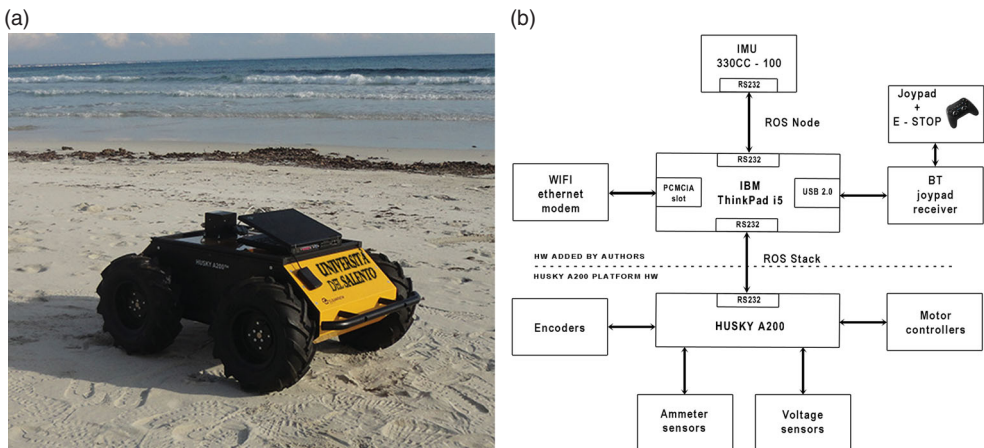


Figure 6. (a) The Husky A200 platform used in all experiments and (b) hardware diagram of the complete system.

4. Experimental results

In order to evaluate the proposed approach for online terrain estimation, field experiments were performed using the 4-wheel drive skid-steer vehicle Husky A200, shown in Figure 6(a). The technical details of Husky are collected in Table 1. The vehicle sensor suite comprises two main types of sensor: motor sensors and inertial sensors. The motor sensors consist of two rotary encoders for measuring the speed of right-hand and left-hand side

Table 1. Technical details of the all-terrain skid-steer vehicle Husky.

Dimensions	$B \times L = 0.6 \text{ m} \times 0.55 \text{ m}$
Wheel diameter	$2r = 0.26 \text{ m}$
Total weight (sensor payload included)	$W = 294.3 \text{ N}$
Motor torque constant	$k_t = 0.044 \text{ Nm/A}$
Gearhead ratio	$\tau = 78.71 : 1$

Note: Please refer to Figures 3 and 5 for more details.

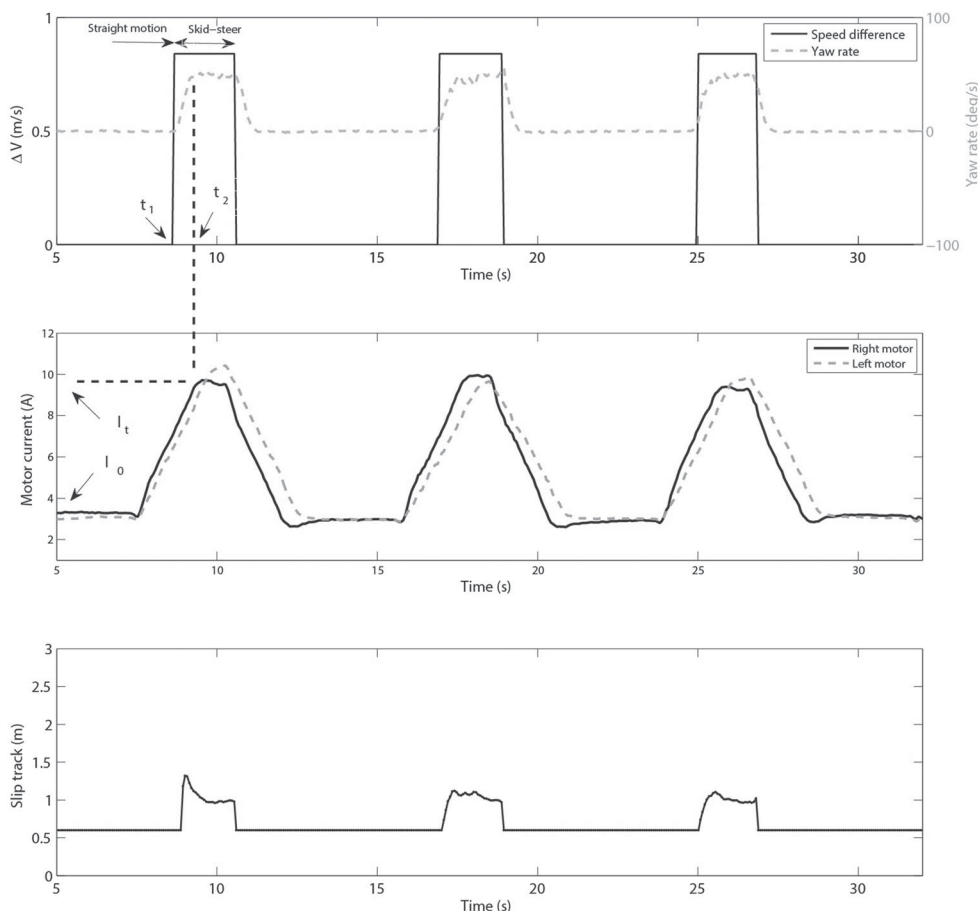


Figure 7. Terrain estimation on asphalt during a 4-m squared path. (a) Vehicle rate-of-turn and speed difference between right-hand and left-hand side wheels, (b) motor electrical currents, and (c) slip track estimation.

wheels and thus their difference (ΔV), two electrical current and two voltage sensors for measuring mechanical torque and momentary power consumption for the left-hand and right-hand side wheels. It should be said that, while Husky features two wheels per side, each side wheel pair is mechanically coupled via a timing belt and commanded by a single drive motor. A six-degree-of-freedom inertial measurement unit Crossbow IMU300CC was used. It comprises three micro electro-mechanical systems accelerometers that use differential capacitance to sense acceleration, and three angular rate sensors consisting of vibrating ceramic plates that utilise the Coriolis force to output angular rate independently of acceleration. Firmware inside the IMU onboard processor produces calibrated angular rate measurements, calibrated acceleration measurements, and estimated navigation state which includes body attitude (i.e. Euler angles: roll, pitch, yaw) using an extended Kalman filter trajectory correction approach.[23]

Data acquisition and processing codes were developed under ROS meta-OS running on a laptop computer. Figure 6(b) shows a block diagram of the hardware architecture.

4.1. Terrain characterisation

During the experiments, the vehicle was commanded to follow two main motion primitives: straight line driving at a constant speed of 0.5 m/s and turn-on-the-spot with a constant rate of turn of about 45 deg/s. Tests were performed on different surfaces: asphalt,

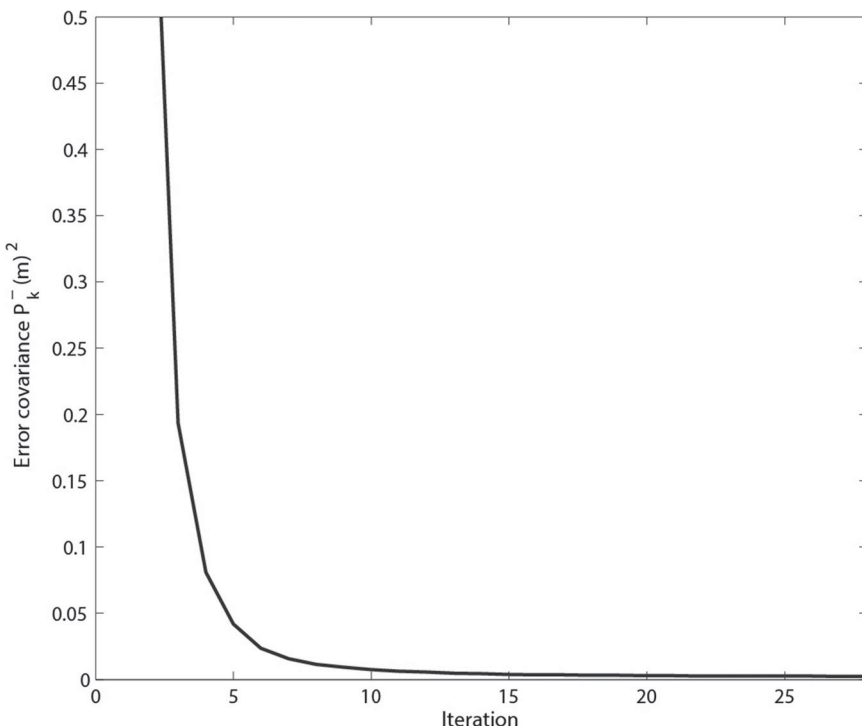


Figure 8. Convergence of the Kalman observer expressed as error covariance P_{k+1}^- versus the iteration.

dirt road, plowed soil and beach sand. Figure 7 shows a sample log of the sensory data during a run on asphalt. In this experiment, Husky completed a 4 m-squared path alternating straight driving and 90 deg-turns to close the loop, as shown by the upper graph of Figure 7, where the rate-of-turn (denoted by a dashed grey line) and the speed difference between the right and left side wheels (marked by a solid black line) are plotted as a function of time. The graph in the middle of Figure 7 refers to the corresponding electrical currents drawn by the motors of the right (black line) and left (dashed grey line) side wheels. Two important parameters can be obtained from this graph, which are strongly correlated with the type of surface. The first parameter is the average electrical current, I_0 , delivered by the drive motors during straight motion at constant speed. In Section 3.1, it was shown that I_0 can be considered as proportional to the coefficient of motion resistance, f_r , that is, $f_r = \tau k_t I_0 / r F_z$.

The second parameter derives from the vehicle response during steady-state cornering. Between the application of differential wheel velocities (time t_1 in the upper plot of

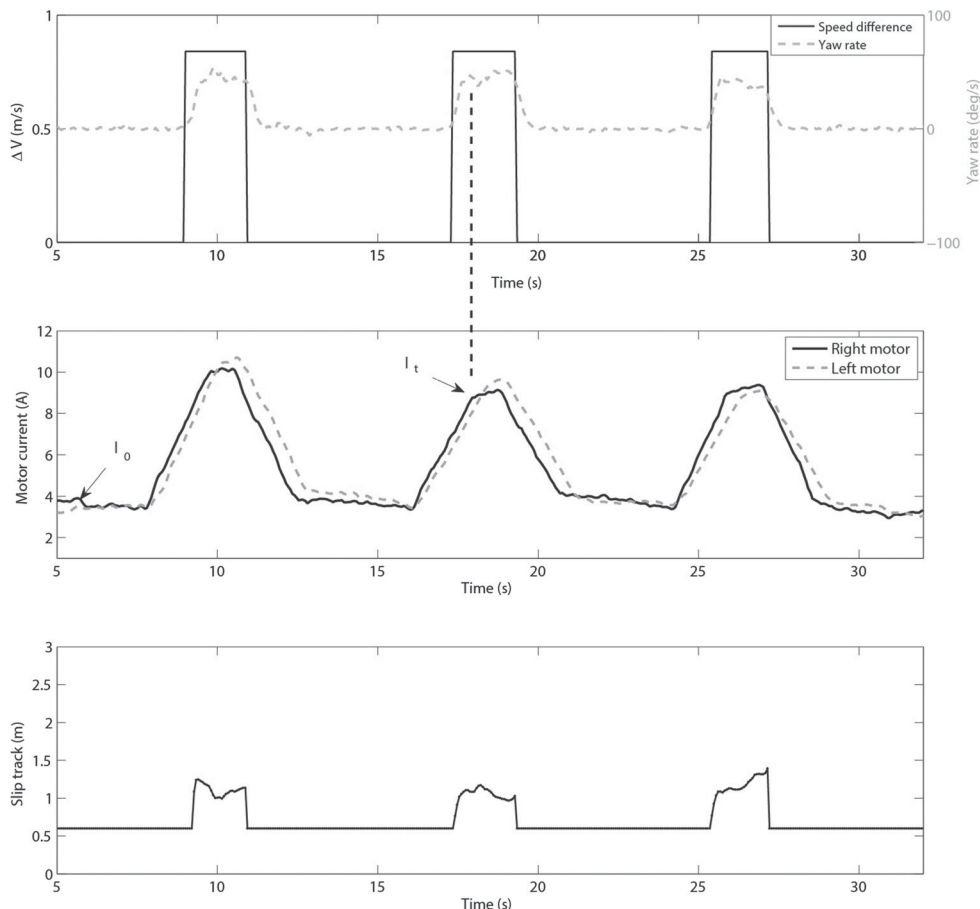


Figure 9. Terrain estimation on dirt road during a 4-m squared path. (a) Vehicle rate-of-turn and speed difference between right-hand and left-hand side wheels, (b) motor electrical currents, and (c) slip track estimation.

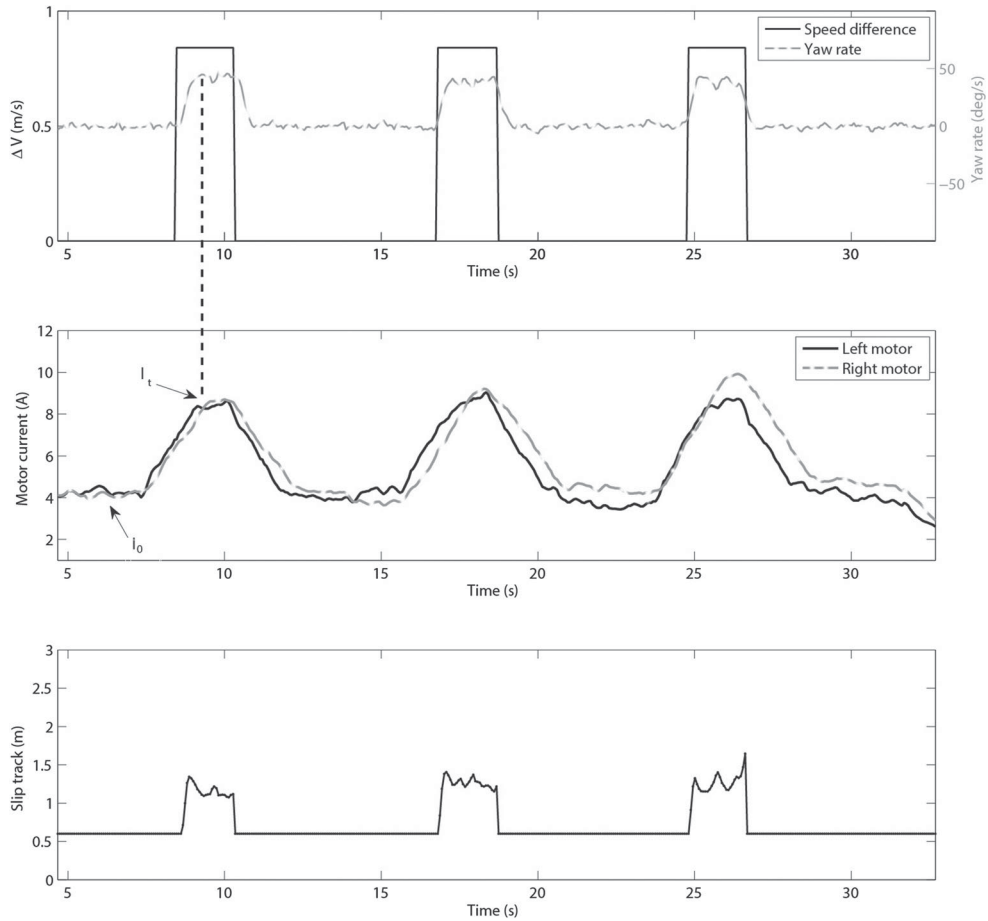


Figure 10. Terrain estimation on plowed agricultural terrain during a 4-m squared path. (a) Vehicle rate-of-turn and speed difference between right-hand and left-hand side wheels, (b) motor electrical currents, and (c) slip track estimation.

Figure 7) and the attainment of steady-state cornering (time t_2), the vehicle is in a transient state. The value of the motor current, I_t , that marks the onset of steady-state is used as the second parameter, which is related to the turning resistance μ_t , according to Equation (27).

Finally, the bottom graph in Figure 7 shows the estimate of the slip track provided by the Kalman filter. It is recalled from Section 2.1 that the observer is active during turning maneuvers, whereas it is switched off for straight driving. In Figure 8 the convergence of the filter during the first 90 deg-turn is discussed in terms of error covariance prediction P_{k+1}^- versus the iteration. By the 12th iteration, it has settled to approximately $0.0025 \text{ (m}^2)$.

Similar experiments were repeated on dirt road, plowed terrain and beach sand. Sample results are collected in Figures 9–11, respectively.

Again, the upper plot shows the rate-of-turn and the speed difference between the left-hand and right-hand wheels of the vehicle, whereas the motor currents and the slip track estimation are shown in the middle and bottom graph, respectively. As can be seen from these figures, the response of the vehicle is generally affected by the type of terrain. In

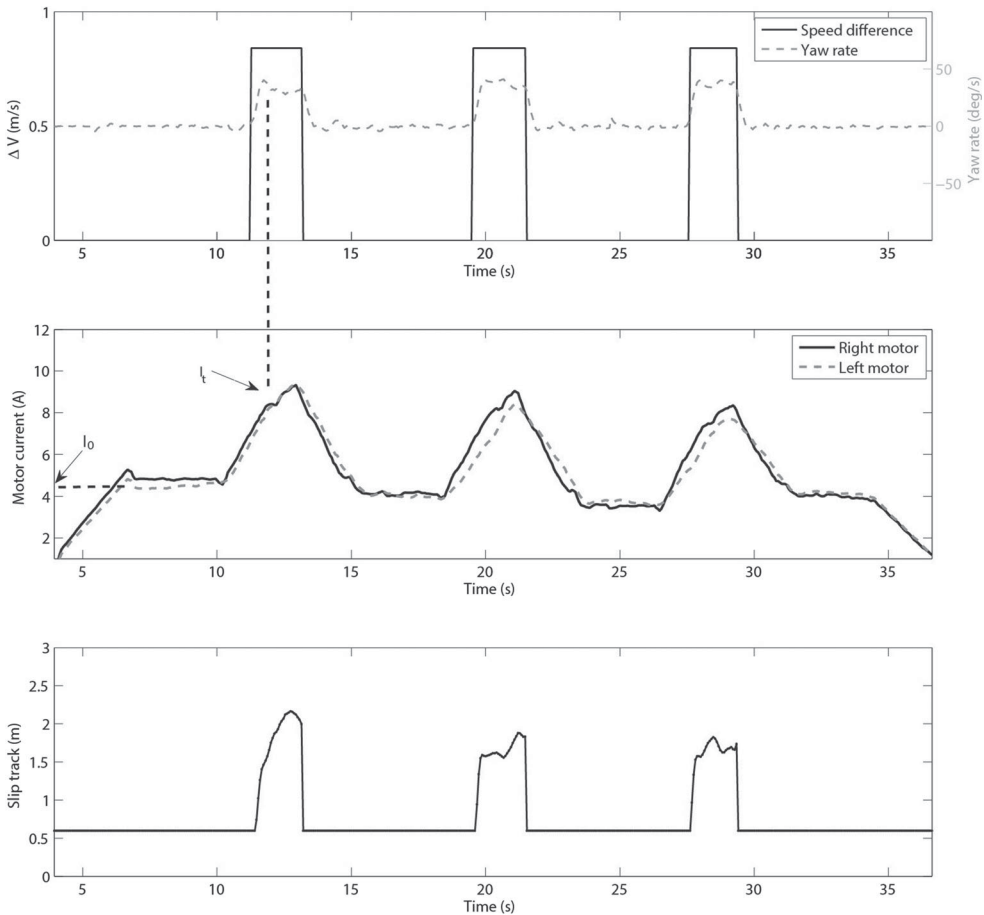


Figure 11. Terrain estimation on beach sand during a 4-m squared path. (a) Vehicle rate-of-turn and speed difference between right-hand and left-hand side wheels, (b) motor electrical currents, and (c) slip track estimation.

detail, the motion resistance f_r is lower on asphalt than on dirt road, plowed terrain and sand. Conversely, the lateral motion resistance μ_t is higher on asphalt than on dirt road, plowed terrain and sand. As a direct consequence, the slip track results larger for beach sand than plowed terrain, dirt road and asphalt.

4.2. Feature space analysis and terrain classification

The proposed approach for online terrain estimation aims to measure the three parameters f_r , μ_t , and B_s , during normal operations. f_r can be estimated in straight line motion, whereas μ_t and B_s are measured during skid-steering. By performing a motion sequence comprising these two primitives, an experimental observation can be obtained as a point in the space (f_r, μ_t, B_s) . The results obtained from repeated tests on different types of terrain are shown in Figure 12. Six runs are repeated for each terrain type. Table 2 summarises the same results in numerical form along with their statistical spread.

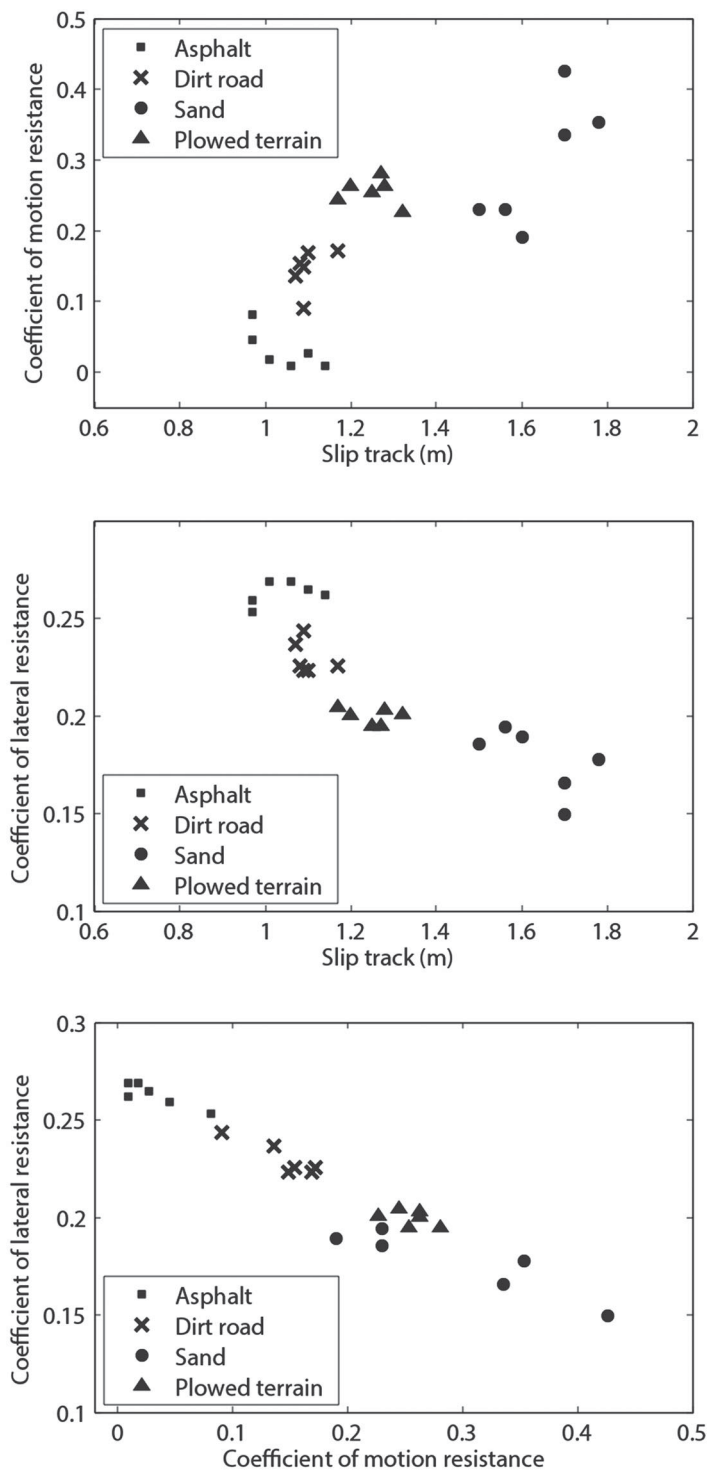


Figure 12. Online terrain estimation based on the measurement of the coefficient of motion resistance, coefficient of lateral resistance and slip track.

Table 2. Online terrain estimation.

	Asphalt –	Dirt road –	Plowed terrain –	Beach sand
Mean f_r	0.03	0.13	0.21	0.30
St. Dev. f_r	0.02	0.03	0.05	0.10
Mean μ_t	0.26	0.20	0.16	0.11
St. Dev. μ_t	0.01	0.02	0.01	0.02
Mean B_s	1.00	1.15	1.26	1.62
St. Dev. B_s	0.05	0.04	0.06	0.09

Note: Results obtained over six repeated runs on each surface.

Table 3. Degree of confidence (high, medium, and low) for terrain characterisation of the three features f_r , μ_t , and B_s .

	Asphalt –	Dirt road –	Plowed terrain –	Beach sand
f_r	High	High	Low	Medium
μ_t	High	High	Medium	Medium–High
B_s	Medium	Low	Medium	High

Table 4. Set of classification rules for terrain classification.

Class	f_r	μ_t	B_s
Asphalt	< 0.1	> 0.25	–
Dirt road	0.1–0.19	0.21–0.25	1–1.2
Plowed terrain	0.2–0.3	0.18–0.21	1.2–1.4
Beach sand	> 0.2	–	> 1.4

The following considerations can be drawn. The slip track B_s can be effective in detecting sand for large values ($B_s > 1.4$), no matter what the other two features are. Similarly, B_s is useful to discriminate instances of asphalt and plowed terrain corresponding, respectively, to $B_s \leq 1$ and $B_s = [1.2, 1.4]$. However, discrimination between asphalt and plowed terrain is less clear in the range of 1 to 1.2. It is also difficult to detect correctly dirt road.

The coefficient of motion resistance f_r increases with the terrain deformability. Therefore, low f_r (< 0.1) strongly indicates the presence of asphalt. Conversely large f_r (> 0.3) points clearly to sand. Motion resistance on dirt road is limited to the range $f_r = [0.1, 0.2]$. Plowed terrain and sand partially overlap between 0.2 and 0.3.

Finally, the coefficient of lateral resistance decreases with the terrain deformability. Large ($\mu_t > 0.25$) and low ($\mu_t < 0.17$) values clearly point to asphalt and sand, respectively. Dirt road can be successfully singled out in the range [0.21, 0.25]. However, discrimination between plowed terrain and sand is less precise in [0.17, 0.21].

To summarise, Table 3 collects advantages and disadvantages of each feature expressed in terms of degree of confidence (high, medium, and low) we have that the given feature can successfully characterise a specific terrain. This feature set expresses our physical understanding of the problem and we believe that it is a good descriptor of the vehicle-terrain interaction.

With reference to Figure 12, a classifier can be constructed that works for this vehicle. For instance, the logical ‘expert system’ described in Table 4 can be adopted.

In order to validate the proposed classification strategy, preliminary experiments were performed driving Husky along pre-programmed paths on mixed terrains. In the first experiment, the vehicle followed a closed-loop path, as shown in Figure 13(a) overlaid over an aerial image taken from Google Earth ($39^{\circ}51'3.30''\text{N}$, $18^{\circ}10'50.98''\text{E}$). In this test,



Figure 13. Field experiments along mixed-terrain paths to validate the proposed terrain classifier: (a) asphalt and sand ($39^{\circ}51'3.30''N, 18^{\circ}10'50.98''E$), and (b) dirt road and plowed terrain ($40^{\circ}3'35.08''N, 18^{\circ}20'42.57''E$). Please refer to Table 5 for classification results.

Husky encountered two types of terrain, namely sand (denoted by a solid black line) and asphalt (marked by a dashed black line). Along its path, the vehicle was able to form an observation after each turn (i.e. at points P_1 , P_2 , and P_3 in Figure 13(a)) as a point in the space (f_r, μ_t, B_s) and to classify the terrain according to the scheme of Table 4. The experimental observations and the corresponding classification results are collected in Table 5. In all three cases, the terrain was correctly classified.

A second test was performed, in a rural environment, where Husky travelled first on a dirt road (solid line) and then on plowed terrain (dashed line). The path followed by the vehicle is shown in Figure 13(b) overlaid over an aerial image

Table 5. Results obtained from the proposed terrain classifier.

Test 1	Observation (f_r, μ_t, B_s)	Classification	Ground-truth
P_1	(0.91, 0.26, 0.90)	Asphalt	Asphalt
P_2	(0.29, 0.20, 1.70)	Sand	Sand
P_3	(0.08, 0.28, 1.05)	Asphalt	Asphalt
Test 2			
P_1	(0.15, 0.23, 1.10)	Dirt Road	Dirt road
P_2	(0.28, 0.20, 1.20)	Plowed terrain	Plowed terrain
P_3	(0.21, 0.22, 1.29)	Plowed terrain	Plowed terrain

($40^{\circ}3'35.08''N, 18^{\circ}20'42.57''E$). Again, the observations generated by the robot along its path and the corresponding results obtained from the terrain classifier are shown in Table 5. Both terrains were correctly detected, attesting to the feasibility of the proposed approach.

As a final remark, it should be noted that the classification rule set expressed by Table 4 is not unique and new relationships or other techniques (e.g. machine learning) may be applied to further improve the classification outcome. It is also not certain that this classifier will work with another vehicle, or a year later. This requires that the classifier has to be adaptive, which is a critical problem that is not addressed in this research. However, detection of changes in terrain type is still possible.

5. Conclusions

This paper described a method for online terrain estimation using a skid-steer vehicle and common onboard sensors. It is based on the estimation of three parameters that depend on the terrain: coefficient of motion resistance, coefficient of lateral resistance and slip track. These parameters can be estimated during normal driving by monitoring the vehicle motion and the wheel torques exerted on the terrain through the use of an inertial measurement unit and electrical current sensors. A model-based Kalman observer was presented to estimate the slip track with one vertical gyroscope and wheel encoders. The use of virtual sensing allowed a physical quantity that is not directly measurable to be inferred through the use of a physics model.

Merits and drawbacks of each parameter were discussed leading to an expert classifier for terrain classification. Experimental results obtained from an all-terrain skid-steer vehicle were presented to validate the system, showing its potential to detect terrain changes and to discriminate between different types of terrain, including asphalt, dirt road, plowed terrain, and sand.

Future research will be devoted to the development of adaptive classifiers that could be trained off-line using previously explored terrains or self-trained via online adjustment. The system will be also tested in long range and long duration experiments.

Disclosure statement

No potential conflict of interest was reported by the authors.

Funding

The financial support of the ERA-NET ICT-AGRI2 through the grant Simultaneous Safety and Surveying for Collaborative Agricultural Vehicles (S3-CAV) is gratefully acknowledged.

References

- [1] Kragh M, Jorgensen RN, Pedersen H. Object detection and terrain classification in agricultural fields using 3D lidar data. *Lecture Notes in Comput Sci.* **2015**; 9163:188–197.
- [2] Ross P, English A, Ball D, Upcroft B, Corke P. Online novelty-based visual obstacle detection for field robotics. *IEEE International Conference on Robotics and Automation (ICRA)*; 2015 May 26–30; Seattle, WA. p. 3935–3940.
- [3] Reina G, Milella A. Towards autonomous agriculture: automatic ground detection using trinocular stereovision. *Sensors.* **2012**;12(9):12405–12423.
- [4] Milella A, Reina G, Underwood J. A self-learning framework for statistical ground classification using radar and monocular vision. *J Field Robot.* **2015**;32(1):20–41.
- [5] Iagnemma K, Kang S, Shibly H, Dubowsky S. Online terrain parameter estimation for wheeled mobile robots with application to planetary rovers. *IEEE Trans Robot.* **2004**;20(5):921–927.
- [6] Ojeda L, Borenstein J, Witus G, Karlsen R. Terrain characterization and classification with a mobile robot. *J Field Robot.* **2006**;23(2):103–122.
- [7] Brooks CA, Iagnemma K. Vibration-based terrain classification for planetary exploration rovers. *IEEE Trans Robot.* **2005**;21(6):1185–1191.
- [8] Gustaffson F. Slip-based tire-road friction estimation. *Automatica.* **1997**;33(6):1087–1099.
- [9] Yi K, Hedrick J, Lee S. Estimation of tire-road friction using observer based identifiers. *Veh Syst Dyn.* **1999**;31(6):233–261.
- [10] Wang J, Alexander L, Rajamani R. Friction estimation on highway vehicles using longitudinal measurements. *ASME J Dyn Syst Meas Control.* **2004**;126(2):265–275.
- [11] Hahn JO, Rajamani R, Alexander L. GPS-based real-time identification of tire-road friction coefficient. *IEEE Trans Control Syst Technol.* **2002**;10(3):331–343.
- [12] Anderson R, Bevly DM. Estimation of tire cornering stiffness using GPS to improve model based estimation of vehicle states. *IEEE Intelligent Vehicles Symposium*; 2005. p. 801–806.
- [13] Waldron KJ, Kinzel GL. Kinematics, dynamics, and design of machinery. New York: Wiley; 2004.
- [14] Martnez J, Madow A, Morales J, Pedraza S, Garca-Cerezo A. Approximating kinematics for tracked mobile robots. *Int J Robot Res.* **2005**;24(10):867–878.
- [15] Pentzer J, Brennan S, Reichard K. Model-based prediction of skid-steer robot kinematics using online estimation of track instantaneous centers of rotation. *J Field Robot.* **2014**;31(3):455–476.
- [16] Reina G, Gentile A, Messina A. Tyre pressure monitoring using a dynamical model-based estimator. *Veh Syst Dyn.* **2015**;53(4):568–586.
- [17] Welch G, Bishop G. An introduction to the Kalman filter. SIGGRAPH; 2001.
- [18] Bekker MG. Introduction to terrain-vehicle systems. Ann Arbor: The University of Michigan; 1969.
- [19] Reina G, Foglia M, Milella A, Gentile A. Visual and tactile-based terrain analysis using a cylindrical mobile robot. *Trans ASME J Dyn Syst Meas Control.* **2006**;128(1):165–170.
- [20] Reina G, Ojeda L, Milella A, Borenstein J. Wheel slippage and sinkage detection for planetary rovers. *Trans Mechatronics.* **2006**;11(2):185–195.
- [21] Kumar V, Waldron K. Force distribution in closed kinematic chains. *IEEE Trans Robot Autom.* **1988**;4(6):657–644.
- [22] Wong J. Theory of ground vehicles. Hoboken, NJ: Wiley; 2008.
- [23] North E, Georgy J, Tarbouchi M, Iqbal U, Noureldin A. Enhanced mobile robot outdoor localization using INS/GPS integration. In: International Conference on Computer Engineering & Systems, Cairo; 2009.